Scientific Visualization, 2023, volume 15, number 4, pages 1 - 11, DOI: 10.26583/sv.15.4.01

Computer Vision Study of the Flow Generated by a Sliding Discharge

I.A. Znamenskaya[1], I.A. Doroshchenko[2], N.N. Sysoev[3]

Lomonosov Moscow State University

[1] ORCID: 0000-0001-6362-9496, znamen@phys.msu.ru
[2] ORCID: 0000-0002-0488-0020 , doroshenko.igor@physics.msu.ru
[3] ORCID: 0000-0002-1162-7680, nn.sysoev@physics.msu.ru

Abstract

A quantitative study has been made of the flow with shock waves generated in air by a sliding surface discharge lasting less than one microsecond. The high-speed flow was visualized using the shadowgraph method, the process was recorded at a rate of 124 000 frames/s, the exposure time was 1 μs. The aim of this work is to study the dynamics of the two discontinuities: the cylindrical shock wave and the contact surface generated by the discharge. Each experiment allowed several hundred images to be taken of a short-lived gas-dynamic process lasting up to 1 ms. A YOLOv8 convolutional neural network was trained and used to determine the positions of the discontinuities. A data set of 984 markups was labeled. The model on the mAP50 metric achieved 0.887 and the mAP50-95 was 0.557. The model was used to automatically measure the vertical dimensions of the contact discontinuity. It expands at times up to 0.4 - 0.8 ms to a vertical size of 5 - 11 mm. The x-t plots and the velocities of the cylindrical shock waves were measured. It is shown that up to 1 ms after the discharge, the flow development is due to the blast wind motion behind the shock wave. It is shown that the use of computer vision can significantly speed up the analysis of high-speed flow visualizations and the extraction of quantitative information.

Keywords: sliding surface discharge, blast wave, contact discontinuity, flow visualization, computer vision, convolutional neural networks.

1 Introduction

1.1 Computer vision and deep learning methods

Computer Vision (CV) is a field of artificial intelligence (AI) that focuses on methods for extracting data from visual sources of information. CV commonly refers to tasks involving the detection, tracking, and classification of objects in digital images. CV is employed to address a wide range of scientific and business challenges, including the development of AI for transportation, analysis of road traffic and road conditions, automatic analysis of medical images (MRI, X-rays), defect detection in manufacturing plants, automated waste sorting, text recognition, barcode scanning, recognition of various objects, and more. Despite CV having its origins in the 1960s, it reached its greatest advancements after 2012 when the convolutional neural network, AlexNet [1], decisively won the ImageNet image recognition competition.

CV methods are frequently applied to address scientific challenges in the analysis of experimental images. They enable the enhancement of image quality, identification of specific objects in images, object segmentation, noise reduction, and the application of various filters. CV is employed to solve tasks such as: converting images to grayscale and black-and-white based on a specified threshold, morphological transformations, gradient computation, edge and contour detection, corner detection, feature extraction, histogram equalization, template

matching, image segmentation, background subtraction, and more. Deep machine learning methods significantly improve the quality of solutions for tasks such as image classification, object recognition, segmentation, image restoration, and style transfer.

This paper presents the results of research of the gas-dynamic flow generated after a pulsed discharge sliding along the surface of a dielectric. The resulting flow was visualized using shadowgraphy and recorded with a high-speed camera. The analysis of a large number of acquired digital images was automated and performed using a deep learning model - a convolutional neural network. The task was to recognize certain flow structures and measure their size.

1.2 Visualization of flows in a gas dynamic experiment and the object of study

Currently, the most common methods for visualizing flows are shadowgraphy and schlieren techniques [2-3], which are based on the phenomenon of light refraction. According to the well-known Gladstone-Dale relation (1), the refractive index of a medium, n, is directly proportional to its density, ρ. This allows for the visualization of density variations in a transparent medium (liquid or gas):

$$n - 1 = G(\lambda)\rho, \quad (1)$$

where G is the Gladstone-Dale constant, and λ is the wavelength of the radiation.

Based on the optical setup of shadowgraphy or schlieren methods, the evolution of flow inhomogeneities can be recorded using digital cameras and other equipment. The images of these inhomogeneities are regions with brightness different from the background. In particular, a shadowgraph image of a shock wave consists of alternating dark and light stripes. The advent of modern high-speed digital cameras has enabled the capture of flows at speeds of up to 10 000 000 frames per second and the accumulation of large volumes of visual data. Consequently, there is a need for automating the processing of the acquired image and video datasets. To address this task, both classical computer vision algorithms [4] and contemporary methods based on convolutional neural networks and deep learning [5] are employed.

In this study, the object of investigation was the non-stationary shockwave flow generated by a nanosecond surface discharge of cylindrical shape. This flow includes a cylindrical shock (blast) wave and a contact surface (CS) propagating from the discharge region. Flows of this type arise, for example, in the case of the breakdown of a pulsed optical discharge induced by focused laser radiation [6] near a solid wall. In [6], the authors conducted experimental research and numerical modeling of the optical discharge near a solid surface. The distance between the focus (discharge area) and the wall was 5 mm. To simulate the flow, the Euler equations were numerically solved, using a model of instantaneous energy deposition defined within a sphere with a radius of 3 mm. It was demonstrated that the dynamics of the resulting shockwave are similar to those of a shockwave generated by a point source explosion. The authors also showed that the CS, which separates the laser-heated gas from the air behind the shockwave front, becomes unstable and develops Rayleigh-Taylor instabilities. Similar flows occur on larger scales, such as in explosions. In [7], numerical simulations were conducted for a 16 kT explosion at an altitude of 580 m above the ground. The energy deposition was defined within a spherical region with a diameter of 2.4 m. Both the descending and reflected shockwaves were simulated, including the resulting rising mushroom-shaped cloud. It was demonstrated that the development of the mushroom-shaped flow is primarily influenced by three factors: the flow behind the shockwave front induced by pressure differences, the rise of the heated region (with a density approximately 700 times lower than that of the surrounding air for t < 10 s), and the motion of vortex rings behind the reflected shockwave.

Similar configurations were observed during the development of high-current nanosecond surface discharges [8]. Mushroom-shaped vortex formations originating from regions of increased energy deposition in the plasma sheets were visualized, evolving from the bottom

wall of the discharge chamber. Through manual image processing, approximately 60 values of the upper coordinates of these formations were obtained.

1.3 Application of computer vision and machine learning methods to solve problems in gas dynamics and flow visualization

To process flow visualization and extract quantitative information, classical computer vision methods are often applied. These methods include edge detection using various algorithms [9-10], the Hough transform for detecting straight lines, typically corresponding to shockwaves and other types of gas dynamic discontinuities [4, 11]. Cross-correlation and template matching algorithms are also used to track the movement of specific flow structures [12]. The Particle Image Velocimetry (PIV) method is based on these algorithms, involving seeding the flow with small particles, typically around 1 μm in size, and illuminating selected flow sections with a laser sheet. The velocity field is calculated by measuring the displacement of particles between two consecutive frames.

Machine learning and deep learning methods are increasingly being used for flow visualization. A detailed review on this topic can be found in [5]. Convolutional neural networks such as Resnet, Unet, and IVD-Net have been successfully applied for vortex recognition [13]. A supervised machine learning approach for filling in missing areas in PIV images achieved high accuracy in reconstructing velocity fields in hidden flow regions [14]. Synthetic PIV images were used for training the model, with corresponding velocity vector outputs. Various machine learning methods were employed in reference [15] to extract quantitative information from schlieren images of a rarefied plasma channel. A neural network for detecting different types of vortex traces behind an oscillating aerodynamic profile was developed and applied for classifying three types of traces: 2S, 2P + 2S, 2P + 4S [16]. Models for feature extraction corresponding to shockwaves from large flow data sets, both experimental and numerical, were proposed in [17-18].

2 Experimental facility and experiments

Flow visualization experiments were carried out in a discharge chamber at pressures in the range p = 90 - 100 Torr. The discharge chamber has a rectangular cross section of 24×48 mm². The top and bottom surfaces are made of dielectric material, while the side walls are made of quartz glass for optical access. Pairs of electrodes, each less than 0.1 mm thick, are embedded in the upper and lower walls of the discharge chamber, 30 mm apart. Surface discharges were produced simultaneously on both the upper and lower walls of the discharge chamber. A voltage of 25 kV was applied to the electrodes. The duration of the surface discharge current sliding along the dielectric surface (plasma sheet) was up to 300 ns, and the glow of the discharge plasma lasted up to 1 μs. In the pressure range used, the plasma sheet exhibits non-uniform glow, with increased energy deposition in 1-2 bright channels, both on the upper and lower surfaces of the discharge chamber.

The schematic of the discharge chamber, the discharge and the shock wave flow generated as a result of the pulsed energy deposition are shown in Figure 1. In addition, Figure 1 shows an integral image of the discharge glow taken with a digital camera. The investigated discharge channels appeared as cylindrical formations of low temperature plasma, 30 mm in length, on the dielectric surface [8].

The pulsed surface discharge under study can be considered, from a gas dynamics perspective, as a cylindrically symmetric explosion. An explosion can be defined as an event caused by the release of a significant amount of energy in a very short period of time within a small, localized volume [7]. The studied discharge fits this definition since the duration of gas heating does not exceed several tens of nanoseconds, and the volume of pulsed energy deposition is limited to a cylinder with a diameter of up to 2 mm.

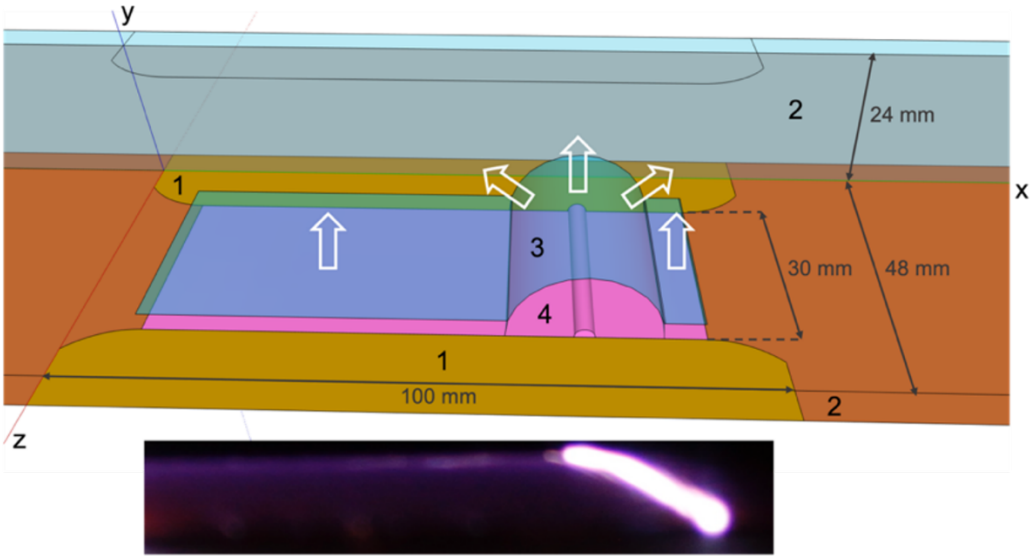

Figure 1 – Experimental setup and integral photo of the pulsed surface discharge. 1 – electrodes, 2 – quartz glass windows, 3 – blast wave, 4 – nanosecond surface discharge

An optical setup was configured to visualize the resulting flow using the shadowgraph method. A parallel beam of light was directed along the discharge channel. At the initial moment, the discharge was initiated. Prior to the discharge, a high-speed camera was triggered to capture shadowgraph images at a rate of 124 000 frames per second. Discharge initiation and camera activation were synchronized by a specially designed electrical circuit.

The aim of the experiment was to obtain shadowgraph frames of the flow generated by the discharges, including the cylindrical shockwaves and the CS, and to measure the diagrams of their motion. The study of the dynamics of the shock waves was carried out manually (as they only appear in a few frames due to their high speed), while a neural network was developed to automatically determine the size of the CS in a large number of frames.

3 Dataset

Figure 2 shows examples of shadowgraph frames obtained at a low chamber pressure of p = 93 Torr and a frame rate of 124 000 frames per second. Shock waves from two discharge channels on the upper and lower walls of the discharge chamber are visible in frames up to 55 μs. Subsequent frames show the evolution of the CS that separates the zone of gas heated by the discharge from the air moving behind the shock wave.

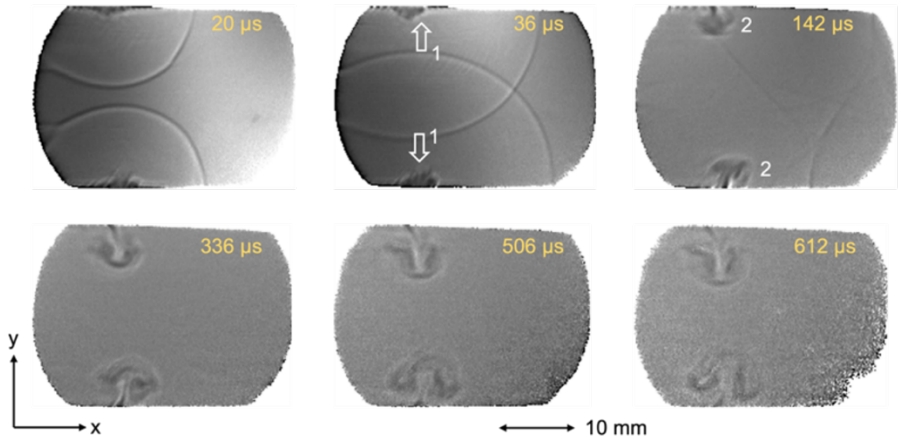

Figure 2 – Shadowgraph images of the main flow stages. 1 – shock wave; 2 – contact discontinuity.

To automatically measure the size of the CS, a dataset was annotated to train a convolutional neural network using the well-known YOLOv8 architecture [19]. The dataset contained objects of a single class, "plume", corresponding to the CS. The dataset consisted of 492 images with 984 annotations. The image size was 368x224 pixels. The image dataset was divided into three groups: a training set (429 images, 87%), a validation set (40 images, 8%) and a test set (23 images, 5%).

The image dataset consisted of both original images taken with a high-speed camera and enhanced versions of these images. New versions of the images were created by applying blurring (up to 2.5 pixels) and adding random noise (up to 5% of pixels). Blurring was applied to make the model more robust to image blurring associated with elongation of the CS along the direction of the probe beam. Adding noise was used to make the model more robust to artefacts in the images.

4 Methods: convolutional neural network for object detection

A YOLOv8 convolutional neural network was used to solve the CS recognition task. At the time of writing, YOLOv8 was the most advanced model, offering an optimal balance between object recognition accuracy and speed. The model showed the best performance on the COCO dataset [20], as measured by the Mean Average Precision (mAP) metric, taking into account the speed of inference (ms/image). A similar model, trained on another set of shadowgraph images containing different flow structures, was used in a previous work [21]. Transfer learning was applied to improve the recognition quality, using weights from a model pre-trained on the COCO dataset. The training process consisted of 95 epochs, and the model hyperparameters were set to default values taken from the Ultralytics repository [22]. The key hyperparameters had the following values: batch = 16, optimiser = SGD (stochastic gradient descent), momentum = 0.937, weight_decay = 0.001.

The following metrics were used to evaluate the model: accuracy, precision, recall, and F_1-score, which is the harmonic mean of precision and recall. These metrics are defined using formulas (2-4) based on the values of TP (true positive – the model correctly classified an object as belonging to the considered class), TN (true negative – the model correctly determined that an object does not belong to the given class), FP (false positive – the model incorrectly classified an object as belonging to the given class), and FN (false negative – the model incorrectly determined that an object does not belong to the given class).

$$precision = \frac{TP}{TP + FP} \tag{2}$$

$$recall = \frac{TP}{TP + FN} \tag{3}$$

$$F_1 = 2 \cdot \frac{precision \cdot recall}{precision + recall} \tag{4}$$

The calculation of object detection model metrics is based on the measurement of overlap. It is determined by the Intersection over Union (IoU) metric, which is the ratio of the intersection and union of predicted regions and ground truth regions on an image. A threshold IoU value was set to determine how much the prediction should overlap with the user annotated ground truth region to be considered correct. If IoU was greater than the threshold, the prediction was considered correct (true positive, TP) and if it was less, it was considered incorrect (false positive, FP). The primary metric used to evaluate the model was the mean average precision (mAP), which is the average of the mean precisions for all classes in the dataset. The average precision for each class (AP) is determined as the area under the precision-recall curve. In addition, metrics such as mAP50, calculated with an IoU threshold of 0.5, and mAP50-95, which is the mAP averaged over the IoU range [0.5 : 0.05 : 0.95], were calculated.

A confusion matrix was also used to assess the performance of the model, which is a table of four different combinations of predicted and actual values.

As a result of the model's predictions for each frame, the corresponding coordinates and sizes of the recognized objects were obtained. Since this work focused on the vertical size of the CS, the heights (h) of the obtained bounding boxes were stored in an array along with their corresponding timestamps (t). A dependency h(t) was constructed. The dependency of the coordinate of the shock wave (y) on time (t), measured manually, was overlaid on the same axes. In some cases, an approximation of the obtained results was performed using polynomials of different degrees chosen based on physical considerations.

5 Results

5.1 Model metrics

The plots for precision-confidence, recall-confidence, precision-recall and F_1-confidence are shown in Figure 3. Figure 4 shows plots of some model metrics, including the most important ones: precision, recall, mAP50 and mAP50-95. After 95 training steps, the mAP50 metric reached 0.887, while mAP50-95 reached 0.557. These are quite good results for a relatively small training dataset. The model was able to detect structures of interest in the flows, such as CS, with an accuracy of up to 1 mm. The detection speed of the model was 13.9 frames/s on a server with the following specifications: Intel(R) Xeon(R) CPU @ 2.00GHz, NVIDIA Tesla T4 16GB GPU, 16GB RAM.

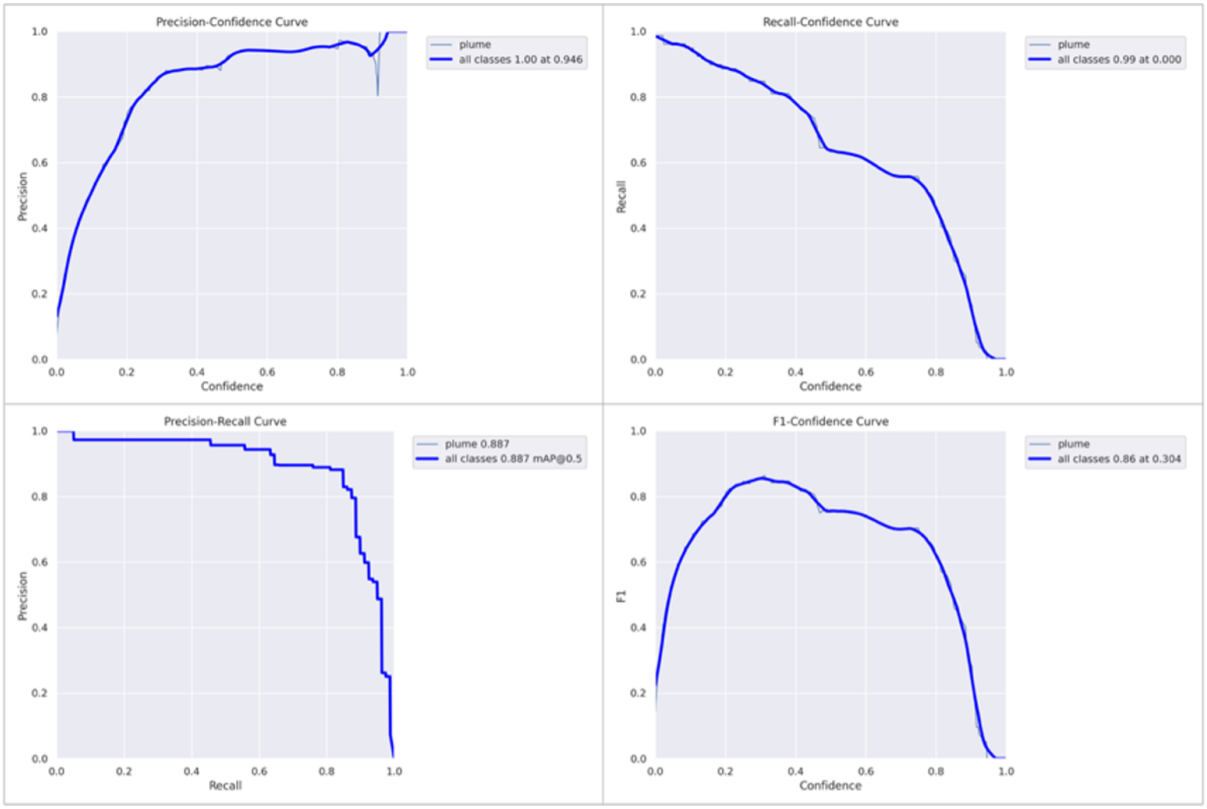

Figure 3 – Model metrics: precision and recall

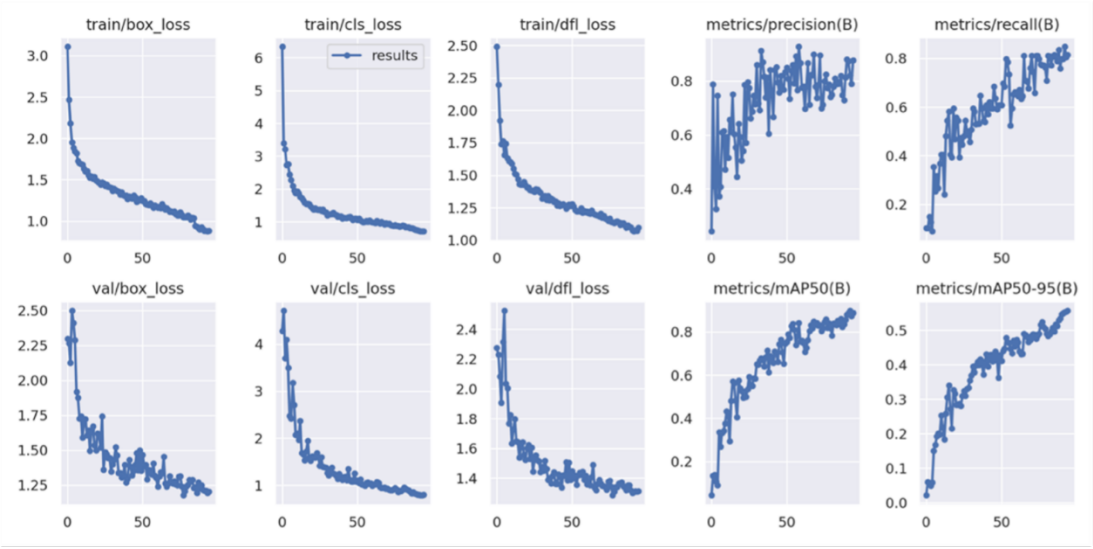

Figure 4 – Model metrics

The confusion matrix of the model (Figure 5) also shows good results. In 90% of cases the model correctly predicted the position of the CS. In 10% of the cases the model made errors where the predicted bounding box for the CS did not match the ground truth by more than the IoU threshold. It's worth noting that the vast majority of errors occurred during the later stages of the flow at t > 0.9 ms, whereas the research objective was to study the flow during the early stages at times up to 1 ms.

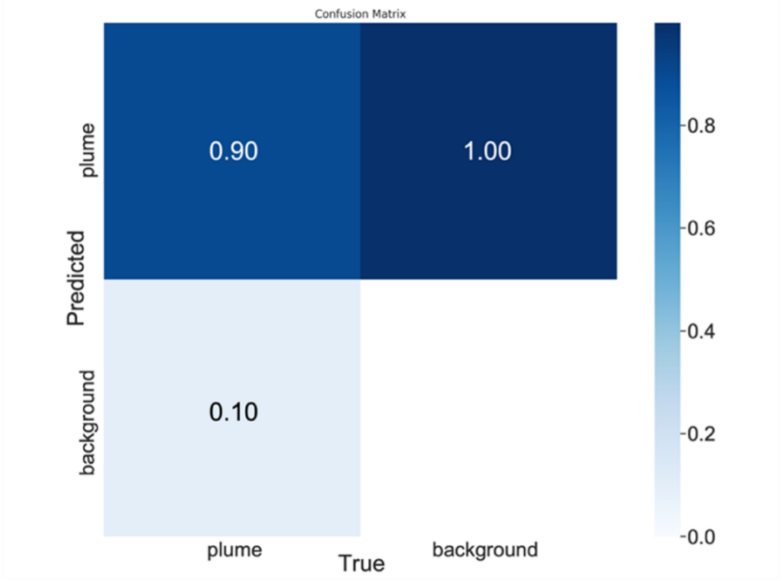

Figure 5 – Confusion matrix

5.2 Flow pattern detection using a convolutional neural network

Figure 6 shows examples of model predictions for frames within the time interval 93 μs to 539 μs. The entire video record of the flow consists of several hundred frames in which the model successfully recognized the CSs. They were successfully identified on both the upper and lower walls of the discharge chamber, including the initial phase of the flow.

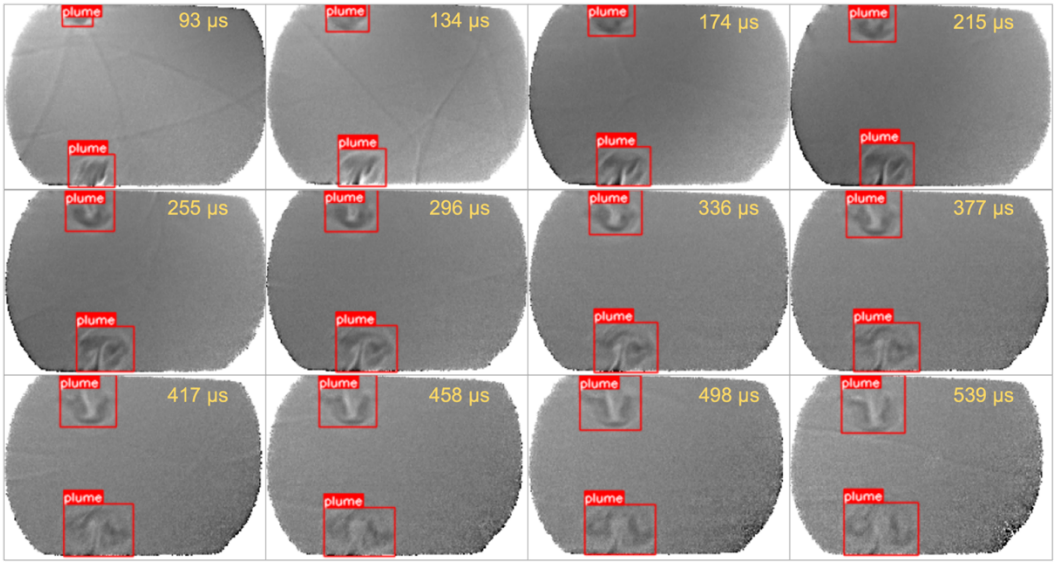

Figure 6 – Contact discontinuity detection

5.3 Analysis of results

The predicted coordinates and sizes of the areas corresponding to the CS were used to automatically construct the size-time dependency, h(t). The corresponding dependencies for two different experiments are shown in Figures 7-8. Each figure includes plots for both the lower and upper CS produced by pulsed discharges on the upper and lower walls of the discharge chamber. Also plotted on the graphs are x-t plots of the resulting cylindrical shock waves. These points were measured manually due to the limited number of images containing shock waves. In Figure 7, the x-t plots of the shock wave motion are separately highlighted in more detail, along with the corresponding second degree polynomial approximations.

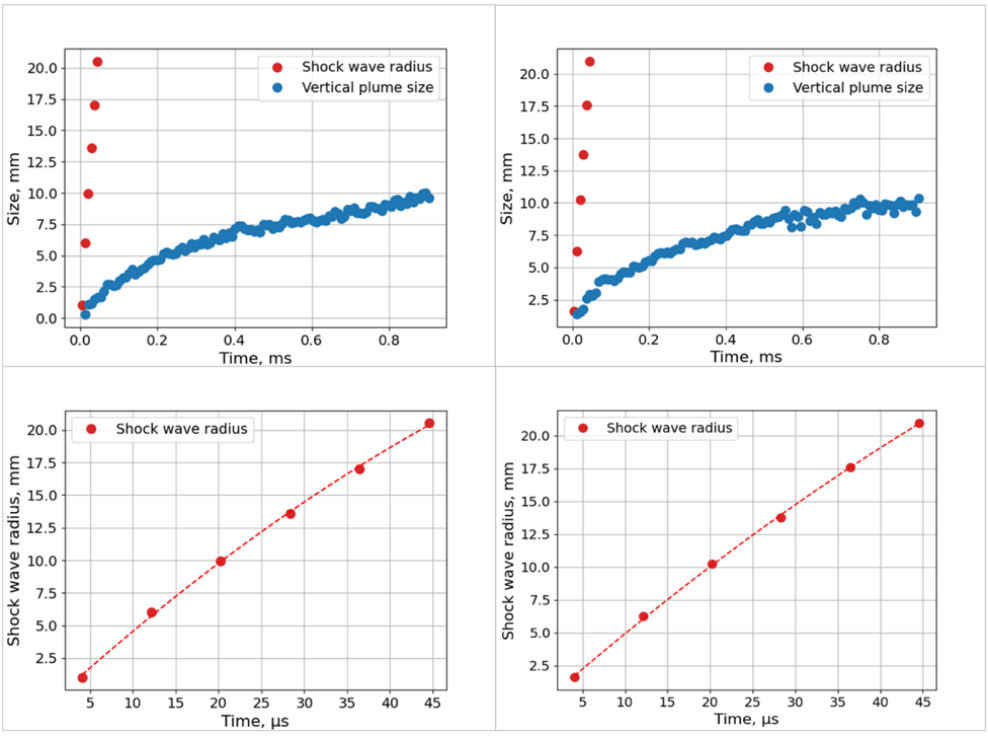

Figure 7 – x-t plots of shock waves and contact discontinuities at 92 Torr pressure. The left column corresponds to the upper flow structures, the right column to the lower ones. The bottom row contains the second order polynomial approximation.

The experiments were carried out under identical conditions except for the pressure in the discharge chamber. In the experiment corresponding to Figure 7, the pressure was 92 Torr. The graphs in Figure 9 correspond to an experiment conducted at a pressure of 99 Torr. Analysis of the plots shows that the speed of the shock waves and the size to which the CS expands depend on the pressure. As the pressure changes, so do the parameters of the discharge and the energy input localised in the plasma cylinder zone. Differences in velocity and degree of gas heating lead to the formation of shock waves of varying intensity. In these experiments, the main factor influencing the development of the CS is the flow behind the shock wave front. Estimates have shown that the influence of gravity (buoyancy) can be neglected when analysing the mechanisms of CS development. Analysis of numerous experimental data has shown that the flow diagrams on the upper and lower walls of the discharge chamber are almost identical.

The difference in diagrams under similar initial conditions is related to random fluctuations in discharge power, energy redistribution between upper and lower discharges, instability, and the significant extent of the CS.

From the data obtained, it can be seen that the shock wave velocity varies little in the observation area and varies between 430 m/s and 480 m/s in different experiments. The CS expands to a vertical size of 5 - 11 mm at times t = 0.4 - 0.9 ms. The final size of the CS and the rate of expansion are greater the higher the velocity of the corresponding shock wave.

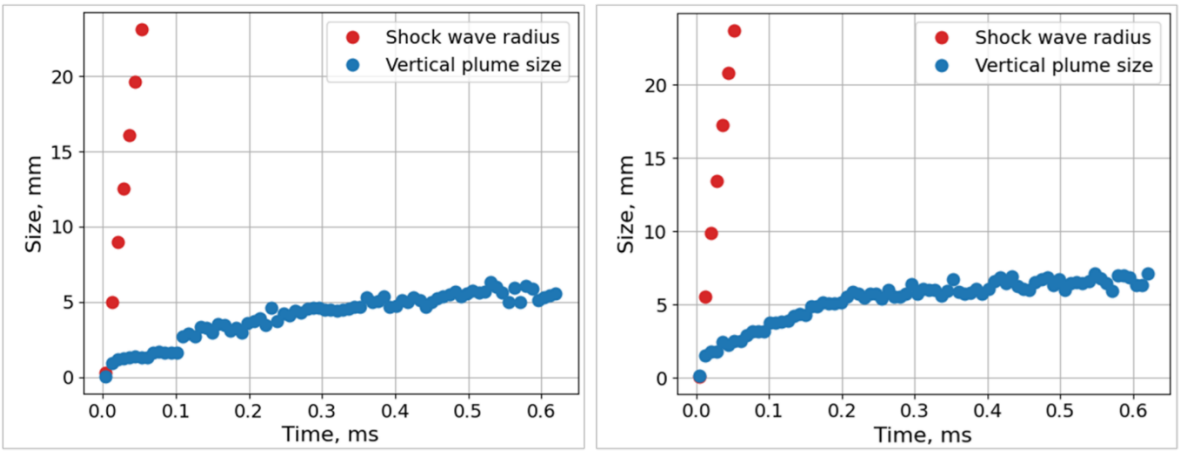

Figure 8 x-t plots of shock waves and contact discontinuities at 99 Torr pressure. The left column corresponds to the upper flow structures, the right column to the lower ones.

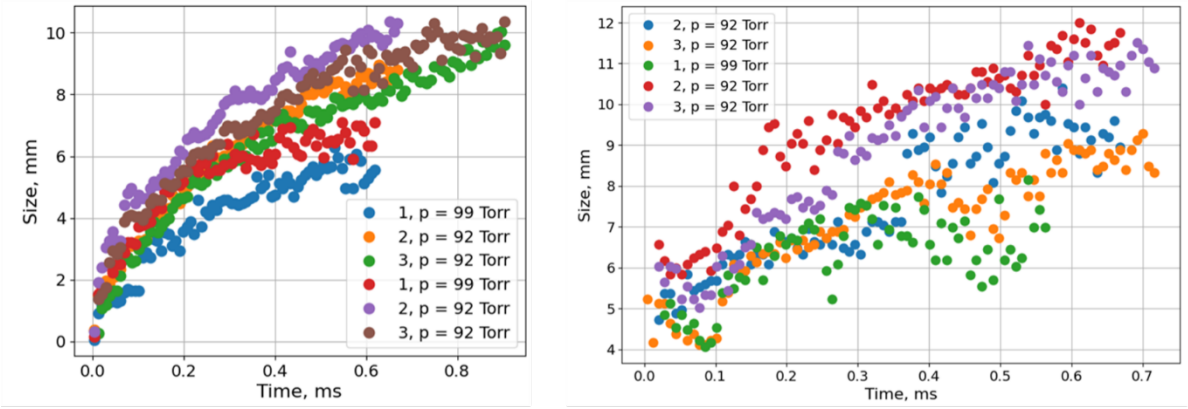

Figure 9. x-t plots of contact discontinuities in the 92-99 Torr pressure range. Left - vertical size. Right - horizontal size.

Based on the x-t plots obtained, by solving the inverse problem, it is possible to numerically calculate the values of the initial energy input - the change in the internal energy of the

gas in the breakdown region. It is also possible to estimate what proportion of the electrical energy was used to heat the gas and form the resulting flow.

Figure 9 shows examples of the automated processing of several video recordings taken over a range of pressures from 92 to 99 Torr. Using the developed model, both the vertical and horizontal dimensions of the CS were measured. It can be seen that as the pressure increases, the vertical extent to which the CS expands decreases. Meanwhile, the horizontal dimensions show little dependence on pressure within the range considered.

6. Conclusions

In this study, shock wave flow generated in air at pressures of 90-100 Torr using sliding surface discharges at an applied voltage of 25 kV was investigated. Flow visualization was performed using the shadowgraph method while probing along the discharge channel. Images were recorded using a high-speed camera at a frame rate of 124 000 frames per second. The aim of the study was to measure the x-t plots of the motion of the resulting cylindrical shock wave and the contact surface over a large dataset of shadowgraph images within a time interval of up to 1 ms.

A convolutional neural network based on the YOLOv8 architecture was successfully trained and applied to detect the region formed after the discharge. The model was trained on a dataset containing 492 shadowgraph images with 984 annotations. The dataset included both the original images captured by the high-speed camera and their enhanced versions created by blurring the original images and adding artificial noise.

The training process consisted of 95 steps, after which the mAP50 metric reached 0.887, and the mAP50-95 reached 0.557. The model's confusion matrix showed that in 90% of cases, the model accurately predicted position of the contact surface. In 10% of cases, the model made errors, with the predicted contact surface bounding box not matching the annotation by an extent greater than the IoU threshold. Most errors corresponded to the later stages of the flow at $t > 0.9$ ms, during blurring and instability development of the contact surface, whereas the research aimed to study the flow up to its cessation on timescales of up to 1 ms.

The trained computer vision model successfully allowed the construction of dependencies of vertical contact surface sizes over time in experiments conducted at different pressures. In addition, x-t plots and velocities of the resulting cylindrical shock waves were measured. The shockwave velocity remained almost constant within the observation region and varied from 430 m/s to 482 m/s over the pressure range studied. The contact surface expanded over time scales of 0.4 to 0.8 ms to a vertical size of 5 to 11 mm. It was shown that for the time scales considered in this study, the influence of gravity (rising of the heated discharge region) can probably be neglected, since the measured flow parameters at the bottom and top of the discharge chamber were identical. Thus, the primary cause of contact surface development is the flow behind the shock front.

The study showed that the application of advanced computer vision methods significantly accelerates the processing of flow visualisations obtained in gas dynamics experiments and speeds up the extraction of quantitative information, providing new physical insights.

7. Acknowledgements

This study was supported by the Russian Science Foundation (Grant No. 22-79-00054), https://rscf.ru/project/22-79-00054/.

References

1. Krizhevsky A., Sutskever I, Hinton G.E. ImageNet Classification with Deep Convolutional Neural Networks // Advances in Neural Information Processing Systems. 2012. T. 25.

2. Settles G.S., Hargather M.J. Review of Recent Developments in Schlieren and Shadowgraph Techniques // Meas. Sci. Technol. 2017. T. 28. № 4.

3. Rienitz J. Schlieren Experiment 300 Years Ago // Nature. 1975. Т. 254. № 5498. С. 293–295.
4. Automatic detection of oblique shocks and simple waves in schlieren images of two-dimensional supersonic steady flows / G. Cammi, A. Spinelli, F. Cozzi, A. Guardone // Measurement. 2021. T 168.
5. Deep learning approaches in flow visualization / C. Liu, R. Jiang, D. Wei, C. Yang, Y. Li, F. Wang & Xiaoru Yuan // Advances in Aerodynamics. 2022. T 4. № 17.
6. Numerical and experimental study of a micro-blast wave generated by pulsed-laser beam focusing / Z. Jiang, K. Takayama, K.P.B. Moosad, O. Onodera, M. Sun // Shock Waves. 1998. Т. 8. С. 337–349.
7. Kim J-H, Kim S. Simulation of Blast Wave Propagation and Mushroom Cloud formation by a Bomb Explosion // AIAA SciTech Forum, 9 - 13 January 2017, Grapevine, Texas, 55th AIAA Aerospace Sciences Meeting. 2017.
8. Shock wave interaction with a thermal layer produced by a plasma sheet actuator / E. Koroteeva, I. Znamenskaya, D. Orlov and N. Sysoev // Journal of Physics D: Applied Physics. 2017. Т. 50.
9. Image Processing Techniques in Shockwave Detection and Modeling / S. Cui, Y. Wang, X. Qian, Z. Deng // J. Signal Inform. Process. 2013. Т. 4. № 3B. С. 109–113.
10. Srisha Rao M.V., Jagadeesh G. Visualization and Image Processing of Compressible Flow in a Supersonic Gaseous Ejector // J. Indian Inst. Sci. 2013. Т. 93. № 1. С. 57–66.
11. Znamenskaya I.A., Doroshchenko I.A. Edge Detection and Machine Learning for Automatic Flow Structures Detection and Tracking on Schlieren and Shadowgraph Images // J. Flow Vis. Image Process. 2021. Т. 28 № 4. С. 1–26.
12. Gena A.W., Voelker C., Settles G.S. Qualitative and Quantitative Schlieren Optical Measurement of the Human Thermal Plume // Indoor Air. 2020. Т. 30. № 4. С. 757–766.
13. Berenjkoub M., Chen G., Günther T. Vortex Boundary Identification Using Convolutional Neural Network // in Proc. 2020 IEEE Visualization Conference (VIS), Salt Lake City, USA, October 25–30. 2020. С. 261–265.
14. Morimoto M., Fukami K., Fukagata K. Experimental Velocity Data Estimation for Imperfect Particle Images Using Machine Learning // Phys. Fluids. 2021. Т. 33. № 8.
15. Machine learning methods for schlieren imaging of a plasma channel in tenuous atomic vapor / G. Bíró, M. Pocsai, I. F. Barna, G. G. Barnaföldi, J. T. Moody, G. Demeter// Optics & Laser Technology. 2023. Т. 159.
16. Colvert B., Alsalman M., Kanso E. Classifying Vortex Wakes Using Neural Networks // Bioinspir. Biomim. 2018. Т. 13. № 2.
17. A Deep Learning Approach to Identifying Shock Locations in Turbulent Combustion Tensor Fields / M. Monfort, T. Luciani, J. Komperda, B. Ziebart, F. Mashayek, G. E. Marai. M.: Springer, Cham, 2017. С. 375–392.
18. Speed detection in wind-Tunnels by processing schlieren images / M. D. Manshadi, H. Vahdat-Nejad, M. Kazemi-Esfeh, M. Alavi, // Int. J. Eng. 2016. Т. 29. № 7. С. 962–967.
19. Real-Time Flying Object Detection with YOLOv8 / D. Reis, J. Kupec, J. Hong, A. Daoudi // arXiv:2305.09972. 2023. С. 1–10.
20. Microsoft COCO: Common Objects in Context / T.-Y. Lin и др. // arXiv:1405.0312. 2014. С. 1–15.
21. Doroshchenko I.A. Analysis of the experimental flow shadowgraph images by computer vision methods // Numerical Methods and Programming (Vychislitel'nye Metody i Programmirovanie). 2023. Т. 24. № 2. С. 231–242.
22. YOLOv8 [Электронный ресурс] / Ultralytics // GitHub. 2023. URL: https://github.com/ultralytics/ultralytics (дата обращения 29.06.2023).